e-Prime - Advances in Electrical Engineering, Electronics and Energy 11 (2025) 100884

Contents lists available at ScienceDirect

e-Prime - Advances in Electrical Engineering, Electronics and Energy

journal homepage: www.elsevier.com/locate/prime

High-precision speed control of induction motors using a multi-pulse voltage source converter and advanced observer-based strategies

Carlos E. Castañeda [a], Antonio Valderrabano-Gonzalez [b,*], Hossam A. Gabbar [c], Vijay K. Sood [c]

[a] Centro Universitario de los Lagos, Universidad de Guadalajara, Lagos de Moreno 47460, Jalisco, Mexico
[b] Universidad Panamericana. Facultad de Ingeniería., Álvaro del Portillo 49, Zapopan, Jalisco, 45010, Mexico
[c] Faculty of Engineering and Applied Science, Ontario Tech University, Oshawa, ON L1G 0C5, Canada

ARTICLE INFO

Keywords:
Sliding mode observer
Asymptotic observer
Luenberger observer
VSC
EMDS

ABSTRACT

This paper presents a speed motor control using a precise Electric Motor Drive System (EMDS) utilizing an 84-pulse Voltage Source Converter (VSC). The development of the VSC signal requires two critical parameters: V_{module}, representing the combined amplitude of the 3-phase signals, and a variable frequency adjusted via a Phase-Locked Loop (PLL) within each sample cycle. To estimate the non-measurable variables (λ_{α_r}, λ_{β_r} and T_L), sliding mode, asymptotic, and Luenberger observers are employed and compared among themselves. The control algorithm is based on sliding mode with an equivalent control strategy, ensuring robust performance under various operating conditions. This control algorithm transforms the plant to be controlled to the non-linear block control form by using error-tracking dynamics. This is to obtain the sliding manifold and to apply the equivalent control strategy. The effectiveness of the proposed system is validated through a set of simulations conducted in Matlab/Simulink, demonstrating its capability to achieve high precision in motor drive applications.

1. Introduction

The development of high-precision Electric Motor Drive Systems (EMDS) is vital for advancing the knowledge in the control of induction motors, which are widely used in various industrial applications. This research focuses on using an 84-pulse VSC to achieve precise speed control of induction motors. The development of the VSC signal relies on two critical parameters: V_{module}, which represents the combined amplitude of the 3-phase signals, and a variable frequency that is dynamically adjusted via a Phase-Locked Loop (PLL). These parameters are essential for an accurate regulation of the motor drive.

To address the challenge of non-measurable variables, this paper integrates sliding modes, asymptotic, and Luenberger observers, which significantly enhance the system's robustness and accuracy. The control algorithm is designed based on sliding modes with an equivalent control strategy [1,2], ensuring stable and precise performance under a wide range of operating conditions. This method effectively handles uncertainties and disturbances, ensuring precise control of the induction motor.

The efficacy of the proposed system is validated through extensive simulations conducted in Matlab/Simulink. The results demonstrate the system's capability to deliver high precision, making it a versatile solution for modern industrial applications. This research contributes to the field of control and power electronics by presenting a robust and efficient framework for high-performance induction motor drives, which fosters further advancements in motor control technology.

The proposal included in [3] outlines a new method, called the enhanced fast terminal sliding-mode observer, designed for wide-speed sensorless control of a Vernier machine used in ship-propulsion systems. Unlike traditional methods that rely on back-electromotive force estimation and PLLs, this approach operates in the dq frame to estimate speed and position without the need for a PLL. This reduces computational load and eliminates the challenges of PLL-based parameter tuning. The article [4] introduces a high-order terminal sliding mode observer (HOTSMO) designed for sensorless control of surface-mounted permanent magnet synchronous motor drives. The HOTSMO addresses challenges like chattering and non-finite-time convergence associated with traditional sliding mode observers. It incorporates a terminal sliding modes surface to achieve finite-time convergence of state variables and employs a high-order sliding modes control law to suppress chattering effectively.

* Corresponding author.
E-mail addresses: carlose.castanedah@academicos.udg.mx (C.E. Castañeda), avalder@up.edu.mx (A. Valderrabano-Gonzalez), hossam.gaber@ontariotechu.ca (H.A. Gabbar), Vijay.Sood@ontariotechu.ca (V.K. Sood).

https://doi.org/10.1016/j.prime.2024.100884
Received 26 July 2024; Received in revised form 13 December 2024; Accepted 16 December 2024
Available online 27 December 2024

Nomenclature	
ASMC	Adaptive Sliding Mode Control.
EMDS	Electric Motor Drive Systems.
HOSMO	High-Order Sliding Mode Observer.
HOTSMO	High-Order Terminal Sliding Mode Observer.
LSLSM	Long Stator Linear Synchronous Motor.
Lo	Luenberger observer.
PLL	Phase-Locked Loop.
Ro	Robust observer.
SMCC	Sliding Mode Current Controller.
Smo	Sliding-modes observer.
SRF	Stationary Reference Frame.
ST-SMO	Super Twisting Sliding Mode Observer.
THD	Total Harmonic Distortion.
VSC	Voltage Source Converter.
V_{module}	Combined amplitude of the 3-phase signals.
v_a, v_b, v_c	3-phase voltages.
v_α, v_β	Stator Voltages in the SRF entering to the EMDS.
$v_{\alpha s}$, $v_{\beta s}$	Stator Voltages in the SRF leaving the EMDS.
i_a, i_b, i_c	3-phase currents.
$i_{\alpha s}$, $i_{\beta s}$	Stator Currents in the SRF.
ω_r, ω_{ref}, $\hat{\omega}_r$	Angular speed, its reference and its estimator.
ϕ, ϕ_{ref}	Rotor flux square modulus and its reference.
$\lambda_{\alpha r}$, $\lambda_{\beta r}$, $\hat{\lambda}_{\alpha r}$, $\hat{\lambda}_{\beta r}$	α and β rotor flux-linkages and their estimators.
T_L, $\hat{T}_L$	Load Torque and its estimator.
ϵ_ω, ϵ_ϕ	Angular speed and Rotor flux square modulus tracking error.
ϵ_1, ϵ_2, ϵ_3	Angular speed, and α and β Stator current estimator errors.
$\epsilon_{\lambda_\alpha}$, ϵ_{λ_β}	α and β flux linkages estimation errors.

The study developed in [5] presents a comprehensive approach to improve the power factor and regulate the induction motor speed, employing two cascade controllers integrated into an AC/DC/AC power converter system. The first controller utilizes a combination of block control linearization and the super-twisting algorithm to effectively regulate reactive power and maintain DC bus voltage stability. On the other hand, the second controller employs state-feedback linearization and the super-twisting algorithm to manage motor speeds above synchronous levels, responding adeptly to abrupt fluctuations in Load Torque.

Ref. [6] introduces an adaptive sliding mode control (ASMC) strategy enhanced by a modified reduced-order proportional integral observer for precise speed control of permanent magnet synchronous motors in the presence of uncertain disturbances such as parameter variations and external Load Torque changes. The ASMC approach employs a novel sliding mode reaching law to mitigate chattering in the control signal, and shorten the time for the system trajectory to reach the sliding mode surface, enhancing control accuracy and responsiveness.

The work [7] introduces a high-order sliding-mode observer (HOSMO) enhanced with an adaptive gain for speed-sensorless induction motor drives, and is aimed at improving robustness and achieving finite-time convergence in speed estimation across a wide operating range. Existing HOSMOs often struggle while ensuring finite-time convergence, which can lead to performance degradation or instability, especially in the field-weakening range. To overcome this challenge, the proposed method first designs a high-order sliding-mode surface to achieve finite-time convergence of rotor flux estimation in the reference model.

The work [8] proposes the use of an Integral Sliding Mode Controller (ISMC) for speed control of a 3-phase induction motor and its superior performance in terms of accuracy, response time, and robustness. The authors report that these characteristics make an ISMC particularly advantageous for applications in manufacturing processes, industrial automation, and electric vehicles, where precise and reliable motor control is essential.

Ref. [9] proposes a composite current control strategy aimed at enhancing robustness and dynamic tracking performance of the stator current control in a Long Stator Linear Synchronous Motor (LSLSM) used in high-speed maglev train traction systems. The approach combines a Sliding Mode Current Controller (SMCC) with a Sliding Mode Disturbance Observer. Initially, the LSLSM mathematical model in double feed mode is optimized for accuracy and efficiency. Based on this model, the SMCC is then designed, incorporating an improved stability criterion and quantitatively determined switching gain to achieve precise current tracking during stator changeover processes.

Ref. [10] introduces an enhanced Super Twisting Sliding-Mode Observer (ST-SMO) that is designed to overcome challenges associated with conventional methods in estimating induction motor parameters. The conventional ST-SMO is noted for issues such as control delay in trajectory convergence, which diminishes anti-disturbance capabilities and affects estimation accuracy and energy efficiency. In response, the proposed method enhances convergence along the sliding surface by introducing a non-linear sliding mode manifold.

The article [11] presents an observer-based back-stepping controller designed for electro-pneumatic actuators, specifically those used in diesel engines to control variable geometry turbochargers. These actuators are preferred because of their superior force-to-weight ratios but pose challenges due to non-linearities such as air mass flow variations, friction, and aerodynamic forces. The objective of the study is to achieve precise control of the actuator by compensating for friction and aerodynamic forces affecting the variable geometry turbochargers.

On the other hand, drives for motors with low Total Harmonic Distortion (THD) are crucial for enhancing power quality and ensuring efficient operation in industrial applications. VSCs are used in these drives to achieve superior performance. The use of VSCs is not limited to motor drives, but the applications can be extended to STATCOMs, active filters, electric vehicles, renewable energy, and uninterruptible power supplies, among others [12]. Nevertheless, most of them give high THD in the output due to a low number of pulses or levels being used in the selected topology.

The strategy proposed in [13], demonstrates that with the use of good planning of the speed trajectory, the control design can be substantially improved in terms of energy used and precision of the movement. The incorporation of the present study can help to increase the flexibility of the system presented here.

This proposal aims to enhance motor speed control by utilizing a precise EMDS equipped with an 84-pulse VSC as the power electronics converter. The development of the VSC signal involves two crucial parameters: one determining the combined amplitude of the 3-phase signals, and another regulating the variable frequency using a PLL. To address the challenge of estimating non-measurable variables such as $\lambda_{\alpha r}$, $\lambda_{\beta r}$, and T_L, this study employs sliding-mode, asymptotic, and Luenberger observers. These observer techniques are compared to assess their effectiveness in accurately estimating these variables, crucial for optimizing motor performance. The control algorithm employed is based on sliding mode principles enhanced by an equivalent control strategy, which ensures robust performance across diverse operational scenarios. This strategy transforms the plant dynamics into a non-linear block control form [14] through error-tracking dynamics, enabling the derivation of a sliding manifold for precise control. Extensive Matlab/Simulink simulations are conducted to rigorously evaluate the

proposed system's capability to achieve high precision in motor drive applications.

This paper is organized as follows: Section 2 provides a comprehensive overview of the design aspects of an advanced electric motor drive system. The paper covers critical components such as the transformation of reference frames, implementation of sliding mode control techniques, integration of robust control strategies, and the utilization of sliding modes, asymptotic and Luenberger observers for state variables, and external disturbance. Additionally, the section details the application of an equivalent control algorithm, highlighting its role in enhancing system performance and robustness. Together, these methodologies contribute to the development of an efficient electric motor drive capable of meeting stringent performance requirements for diverse operational conditions.

Section 3 presents a comprehensive evaluation of the proposed control and observer strategies. It provides a detailed insight into the design methodology and simulation results, focusing on the performance and effectiveness of the observers in tracking the controlled variables. Statistical analyses are included to assess the accuracy of the estimated variables and their impact on overall tracking performance.

Lastly, Section 4 presents the key conclusions drawn from this study. It synthesizes the main outcomes and contributions of the proposed approach, highlighting its efficacy and implications for practical applications.

2. Design of an efficient electric motor drive system

2.1. Stationary reference frame transformation

The coordinate reference for the 3-phase power system is a 3-axis system with a 120-degree phase shift. However, to facilitate the control algorithm implementation and analyses, the adoption of orthogonal coordinates is deemed preferable.

In this paper, the transformation matrix used is the standard (Amplitude-Invariant) Clarke transformation to position the coordinates in the Stationary Reference Frame (SRF) [15,16]. This transformation is defined by Eq. (1).

$$\begin{bmatrix} v_\alpha \\ v_\beta \end{bmatrix} = \frac{2}{3}\begin{bmatrix} 1 & -\frac{1}{2} & -\frac{1}{2} \\ 0 & \frac{\sqrt{3}}{2} & -\frac{\sqrt{3}}{2} \end{bmatrix}\begin{bmatrix} v_a \\ v_b \\ v_c \end{bmatrix} \tag{1}$$

In Eq. (1), v_a, v_b, and v_c are the 3-phase voltages from phase to neutral connection. The adoption of this transformation is convenient because the magnitude of v_α is the same as the magnitude of v_a when the voltages are balanced.

The inverse transformation matrix is defined in Eq. (2),

$$\begin{bmatrix} v_a \\ v_b \\ v_c \end{bmatrix} = \begin{bmatrix} 1 & 0 \\ -\frac{1}{2} & \frac{\sqrt{3}}{2} \\ -\frac{1}{2} & -\frac{\sqrt{3}}{2} \end{bmatrix}\begin{bmatrix} v_\alpha \\ v_\beta \end{bmatrix} \tag{2}$$

The acquisition of v_α and v_β is very important as they are used to synchronize the gate signals and develop the control law for the motor.

The Clarke transformation for currents i_a, i_b, and i_c is utilized to convert them into the SRF currents i_α and i_β, as expressed by:

$$\begin{bmatrix} i_\alpha \\ i_\beta \end{bmatrix} = \frac{2}{3}\begin{bmatrix} 1 & -\frac{1}{2} & -\frac{1}{2} \\ 0 & \frac{\sqrt{3}}{2} & -\frac{\sqrt{3}}{2} \end{bmatrix}\begin{bmatrix} i_a \\ i_b \\ i_c \end{bmatrix} \tag{3}$$

Conversely, the inverse Clarke transformation is represented by:

$$\begin{bmatrix} i_a \\ i_b \\ i_c \end{bmatrix} = \begin{bmatrix} 1 & 0 \\ -\frac{1}{2} & \frac{\sqrt{3}}{2} \\ -\frac{1}{2} & -\frac{\sqrt{3}}{2} \end{bmatrix}\begin{bmatrix} i_\alpha \\ i_\beta \end{bmatrix} \tag{4}$$

is used to transform i_α and i_β back into the 3-phase currents i_a, i_b, and i_c. Eq. (3) facilitates the calculation of i_α and i_β when i_a, i_b, and i_c are measurable, while Eq. (4) serves as its respective inverse transformation.

Table 1
Squirrel-cage induction motor model parameters [16].

Parameter	Value	Units
Stator resistance, R_s.	0.435	Ω
Rotor resistance, R_r.	0.816	Ω
Stator leakage reactance, X_{ls}.	0.754	Ω
Rotor leakage reactance, X_{lr}.	0.754	Ω
Magnetizing reactance, X_m.	26.130	Ω
Inertial moment, J_m.	0.089	kg m^2
Power, P.	3	HP
Line-to-Neutral rated voltages, v_a, v_b, and v_c.	127[a]	V

[a] The voltage indicated in [16] is 220 V Line-to-Line, and it is modified to 127 V Line-to-Neutral for this paper.

2.2. Precise electric motor drive system

A precise EMDS is required for applications where movement and position are crucial, including robotics, Computer Numerical Control machines, electric vehicles, and industrial automation. For the design of the EMDS, it is necessary to know the type of motor, power electronics involved, feedback devices, and controller definition. Required speed, position, and torque values are important to define the complete system. To consider an EMDS as a good system, it should have high precision in controlling speed or position, be efficient in the use of energy, be able to be used for several motor types, and have a long operating life. Precise power electronics topologies are needed to ensure the good behavior of the whole system.

This paper focuses on a specific squirrel-cage induction motor with parameters outlined in Table 1. The motor's characteristics and specifications play a pivotal role in the design and implementation of the EMDS discussed in this study. By addressing the motor's specific requirements and integrating them into the EMDS framework, the paper aims to demonstrate how these components work together to achieve precise control over angular speed and rotor flux square modulus, optimize energy consumption, and ensure robust performance in industrial and automotive applications.

In the design of the controller, it is assumed that the angular speed ω_r, and the currents i_a, i_b, and i_c are directly measurable. These currents are used to compute $i_{\alpha s}$, and $i_{\beta s}$ using Clarke's transformation (3). An 84-pulse VSC-based EMDS is utilized to obtain the voltage signal of variable amplitude and frequency to produce the required currents. However, since the rotor flux linkages $\lambda_{\alpha r}$ and $\lambda_{\beta r}$ are not directly measurable, a sliding-mode observer is designed to estimate these variables. Additionally, a Luenberger observer is designed to make comparisons in the dynamic behavior of the whole system. Also, load torque is estimated using both observers. The block diagram of the proposal is shown in Fig. 1. This diagram illustrates the control and estimation framework for a squirrel-cage induction motor system using sliding mode observers (SMOs) and sliding modes with equivalent control algorithms. Below is a detailed explanation:

1. **Reference Inputs**: Two main reference signals are provided: ω_{ref} (reference angular speed) and ϕ_{ref} (reference for the square modulus of rotor flux linkages).
2. **Tracking Errors**: The tracking errors are obtained by calculating the difference between the reference signals and their corresponding feed-forward values, where the feed-forward value for the angular speed is a measured quantity, and the square modulus of rotor flux linkages is an estimated value. These errors, denoted as $\varepsilon_{\omega_{\text{Smo}}}$ and $\varepsilon_{\phi_{\text{Smo}}}$, serve as inputs to the control system, allowing it to dynamically adjust the control actions to ensure accurate tracking of the desired performance.
3. **Sliding Modes with Equivalent Control Algorithm**: The primary control block employs a sliding mode control algorithm that integrates a VSC-based (Variable Structure Control) equivalent control strategy. This module processes the tracking errors

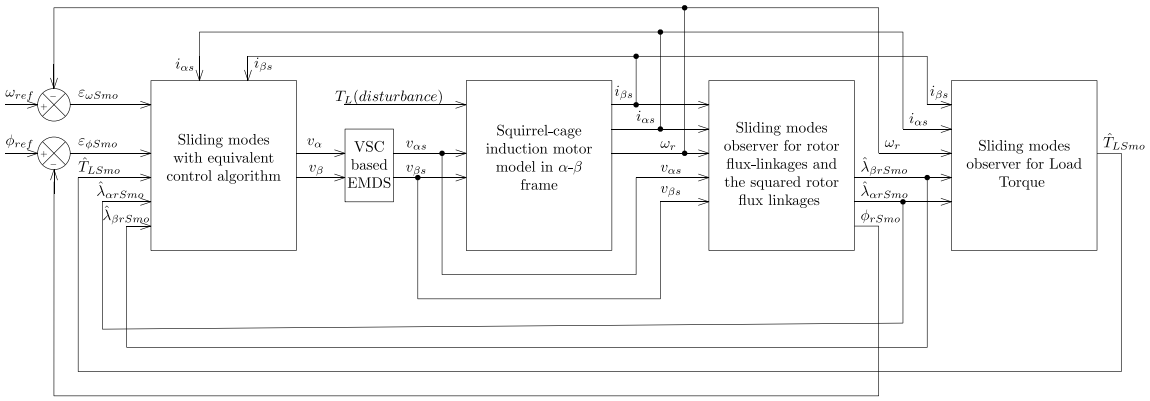

Fig. 1. Block diagram for high-precision speed control proposal.

$\epsilon_{\omega\text{Smo}}$ and $\epsilon_{\phi\text{Smo}}$, the transformed currents $i_{\alpha s}$ and $i_{\beta s}$, as well as the estimated values for the load torque $\hat{T}_{L\text{Smo}}$ and the flux linkages $\hat{\lambda}_{\alpha r\text{Smo}}$ and $\hat{\lambda}_{\beta r\text{Smo}}$. Using this information, the module generates control voltages $v_{\alpha s}$ and $v_{\beta s}$, which are essential for regulating the motor performance and ensuring accurate control of its operation.

4. **Squirrel-Cage Induction Motor Model**: The induction motor is modeled in the $\alpha-\beta$ reference frame, receiving control voltages $v_{\alpha s}$ and $v_{\beta s}$ as inputs, as well as disturbance signals like load torque T_L. The output variables of the motor model include the angular speed ω_r and the currents $i_{\alpha s}$ and $i_{\beta s}$.
5. **Sliding Modes Observer for Rotor Flux Linkages**: This observer estimates the rotor flux linkages $\hat{\lambda}_{\alpha r\text{Smo}}$ and $\hat{\lambda}_{\beta r\text{Smo}}$, as well as the square modulus of rotor flux linkages $\hat{\phi}_{r\text{Smo}}$. These estimations are used in the control and estimation processes to monitor and adjust the system's performance.
6. **VSC-Based Electric Motor Drive System (EMDS)**: An 84-pulse VSC-based EMDS is employed to generate a voltage signal with an adjustable amplitude that is tracked using V_{module}, and frequency that is followed with the use of a PLL, enabling the production of the desired currents.
7. **Sliding Modes Observer for Load Torque**: A dedicated observer estimates the load torque $\hat{T}_{L\text{Smo}}$, which is critical for accurate control of the motor. This estimation is fed back to the control system to refine the control actions.

This setup ensures robust performance against disturbances and parameter variations by leveraging sliding mode control and observers to maintain the desired motor operation.

The control algorithm used in this paper is based on sliding modes with the equivalent control strategy, as presented in [17]. In that paper, the regulation of angular speed with different reference signals and external disturbances was achieved, illustrating the efficiency of the control algorithm with 84-pulses VSC. The EMDS has the role of efficiently converting electrical power into mechanical power, providing precise control of angular speed and rotor flux square modulus of the motor. It includes several electronic stages, being the VSC the main one. To have the VSC provide the required development characteristics, a Neutral Point Reinjection (NPR) technique that involves injecting currents into the neutral point of the DC-link capacitors, is used. This technique provides advantages such as decreasing the harmonic distortion in voltage and current, reducing the total number of switches used to generate the low THD sinusoidal staircase signal, reducing the losses and stress on the switches, enhancement of the overall system efficiency and dynamic performance. Good implementation of the NPR technique in multi-pulses VSC has been demonstrated in [17,18]. In these proposals, two 6-pulse converters are connected in series to establish a neutral point for a conventional 12-pulse inverter. To achieve improved harmonic performance and higher pulse count, a 1-phase 7-level converter is integrated into the system. This converter is connected via its middle voltage point to a reinjection transformer. The 7-level converter operates at a switching frequency six times that of the 12-pulse inverter to always ensure precise frequency and phase alignment for the 3-phase system. The integration of the 7-level converter introduces a pulse multiplication effect, increasing the pulse count to 84. This high pulse count effectively reduces harmonic distortion and improves the overall performance of the inverter system. Details regarding the implementation, including circuit design and configuration, are thoroughly discussed in [19].

Two parameters are needed to manage the EMDS-based 84-pulses VSC, and make it able to track the required voltage for keeping the motor under the desired behavior. The first one is the amplitude of the combined 3-phase signals, known as V_{module}, and defined by (5). It is important to note that this value is a constant for balanced 3-phase systems with constant amplitude, but will change as the set of voltages changes due to the energy management required by the connected motor. So, any modification in the speed or torque of the motor will be reflected in the amplitude V_{module}.

$$V_{module} = \sqrt{v_a^2 + v_b^2 + v_c^2} \tag{5}$$

The second parameter to synthesize the required 3-phase voltage using the EMDS-based 84-pulses VSC is the frequency which varies during start-up of the motor and under torque and velocity-varying operating conditions. Gate signals for controlling the switches of the VSC depend on the correct synchronization of the phase angle of the whole system. A PLL algorithm to follow and adjust phase angles within one sampling cycle to ensure the desired motor performance is discussed in [20–22], and described in Eq. (6).

$$\omega t = 2\left[-tan^{-1}\left(\frac{v_\alpha}{\sqrt{{v_\alpha}^2 + {v_\beta}^2} - v_\beta}\right) + \frac{\pi}{2}\right] \tag{6}$$

2.3. Observer design of flux linkages and load torque

The mathematical model of the squirrel-cage induction motor used in this work is as follows [17]:

$$\begin{aligned}
\frac{d\omega_r}{dt} &= K_T\left(i_{\beta s}\lambda_{\alpha r} - i_{\alpha s}\lambda_{\beta r}\right) - \frac{B_m}{J_m}\omega_r - \frac{1}{J_m}T_L \\
\frac{d\lambda_{\alpha r}}{dt} &= -\frac{1}{T_r}\lambda_{\alpha r} - \frac{P}{2}\omega_r\lambda_{\beta r} + \frac{L_m}{T_r}i_{\alpha s} \\
\frac{d\lambda_{\beta r}}{dt} &= \frac{P}{2}\omega_r\lambda_{\alpha r} - \frac{1}{T_r}\lambda_{\beta r} + \frac{L_m}{T_r}i_{\beta s} \\
\frac{di_{\alpha s}}{dt} &= \frac{\delta}{T_r}\lambda_{\alpha r} + \frac{P}{2}\delta\omega_r\lambda_{\beta r} - \gamma i_{\alpha s} + \frac{1}{\sigma L_s}v_{\alpha s} \\
\frac{di_{\beta s}}{dt} &= -\frac{P}{2}\delta\omega_r\lambda_{\alpha r} + \frac{\delta}{T_r}\lambda_{\beta r} - \gamma i_{\beta s} + \frac{1}{\sigma L_s}v_{\beta s}
\end{aligned} \tag{7}$$

where the state variables considered include: the angular speed ω_r (in rev/min); the α and β rotor flux-linkages $\lambda_{\alpha r}$, $\lambda_{\beta r}$ (in Wb); and the α and β stator currents $i_{\alpha s}$ and $i_{\beta s}$ (in A). The input signals consist of the stator voltages $v_{\alpha s}$ and $v_{\beta s}$ (in V), while the load torque T_L (in N m) represents the external disturbance. Other relevant parameters are detailed in [23,24]. The angular speed ω_r can be accurately measured using an incremental encoder. Measurement of stator currents $i_{\alpha s}$ and $i_{\beta s}$, involves transforming the 3-phase currents i_a, i_b, and i_c that are obtained by using Hall effect current sensors. Unlike these variables, the rotor flux-linkages $\lambda_{\alpha r}$ and $\lambda_{\beta r}$, cannot be directly measured, which makes the use of state observers a requirement. Similarly, the external disturbance T_L is considered non-measurable for this work; thus an estimator has been developed to consider the torque effects of the system.

2.3.1. Sliding modes observer

As mentioned earlier, the rotor flux linkages $\lambda_{\alpha r}$ and $\lambda_{\beta r}$ of the system (7) are non-measurable; then, it is necessary to make an observer for estimating these variables. Thus, using a methodology similar to the one presented in [11], the sliding modes observer is defined as follows:

$$\begin{aligned}
\frac{d\hat{\omega}_r}{dt} &= K_T\left(\hat{i}_{\beta s}\hat{\lambda}_{\alpha r} - \hat{i}_{\alpha s}\hat{\lambda}_{\beta r}\right) - \frac{B_m}{J_m}\hat{\omega}_r - \frac{1}{J_m}\hat{T}_L + \alpha_1\epsilon_1 + k_1\ \mathrm{sign}(\epsilon_1)\\
\frac{d\hat{\lambda}_{\alpha r}}{dt} &= -\frac{1}{T_r}\hat{\lambda}_{\alpha r} - \frac{P}{2}\hat{\omega}_r\hat{\lambda}_{\beta r} + \frac{L_m}{T_r}\hat{i}_{\alpha s} + \alpha_2\epsilon_1 + \alpha_6\epsilon_2 + k_2\ \mathrm{sign}(\epsilon_1)\\
&\quad + k_6\ \mathrm{sign}(\epsilon_2)\\
\frac{d\hat{\lambda}_{\beta r}}{dt} &= \frac{P}{2}\hat{\omega}_r\hat{\lambda}_{\alpha r} - \frac{1}{T_r}\hat{\lambda}_{\beta r} + \frac{L_m}{T_r}\hat{i}_{\beta s} + \alpha_3\epsilon_1 + \alpha_7\epsilon_3 + k_3\ \mathrm{sign}(\epsilon_1)\\
&\quad + k_7\ \mathrm{sign}(\epsilon_3)\\
\frac{d\hat{i}_{\alpha s}}{dt} &= \frac{\delta}{T_r}\hat{\lambda}_{\alpha r} + \frac{P}{2}\delta\hat{\omega}_r\hat{\lambda}_{\beta r} - \gamma\hat{i}_{\alpha s} + \frac{1}{\sigma L_s}v_{\alpha s} + \alpha_4\epsilon_1 + \alpha_8\epsilon_2 + k_4\ \mathrm{sign}(\epsilon_1)\\
&\quad + k_8\ \mathrm{sign}(\epsilon_2)\\
\frac{d\hat{i}_{\beta s}}{dt} &= -\frac{P}{2}\delta\hat{\omega}_r\hat{\lambda}_{\alpha r} + \frac{\delta}{T_r}\hat{\lambda}_{\beta r} - \gamma\hat{i}_{\beta s} + \frac{1}{\sigma L_s}v_{\beta s} + \alpha_5\epsilon_1 + \alpha_9\epsilon_3\\
&\quad + k_5\ \mathrm{sign}(\epsilon_1) + k_9\ \mathrm{sign}(\epsilon_3)
\end{aligned} \tag{8}$$

For this analysis, the symbol $\wedge$ is used to represent the estimated values for each variable. Specifically, these variables are defined as follows: angular speed estimator $\hat{\omega}_r$; rotor flux-linkages $\hat{\lambda}_{\alpha r}$ and $\hat{\lambda}_{\beta r}$ in α-β frame; and alpha and beta current estimators $\hat{i}_{\alpha s}$, $\hat{i}_{\beta s}$. Also, an estimated value for the external disturbance is defined as $\hat{T}_L$.

Additionally, we introduce error terms to quantify the differences between real values and their estimated counterparts. The angular speed estimation error is defined as $\epsilon_1 = \omega_r - \hat{\omega}_r$, and captures the variation between the real angular speed ω_r and its estimated value $\hat{\omega}_r$; stator alpha current estimation error $\epsilon_2 = i_{\alpha s} - \hat{i}_{\alpha s}$, represents the deviation between the real alpha current ($i_{\alpha s}$) and its estimated counterpart $\hat{i}_{\alpha s}$; and stator beta current estimation error $\epsilon_3 = i_{\beta s} - \hat{i}_{\beta s}$ signifies the gap between the real beta current ($i_{\beta s}$) and its estimated value $\hat{i}_{\beta s}$.

The error terms play a crucial role in assessing the accuracy of the measurements, especially considering that the variable ω_r is directly measurable, while $i_{\alpha s}$, and $i_{\beta s}$ are obtained after the transformation (3) of the measured currents i_a, i_b and i_c. So, we focus on the estimation of the variables $\lambda_{\alpha r}$ and $\lambda_{\beta r}$ because they are not measurable. By analyzing the error terms, we gain valuable insights into the performance of our estimation techniques. Also, the term sign($\epsilon_\bullet$) represents the sign of each error ϵ_1, ϵ_2, and ϵ_3. Finally, the constants k_1, k_2, …, k_9 are arbitrary positive constants, and α_1, α_2, …, α_9 are positive constant values that ensure the convergence of the observer which is presented in Appendix A.

Emphasizing the methodology used in this work to propose the observer model (8), the process unfolds in the following crucial steps:

- Based on the motor model (7), the general structure of the observer (8) is proposed.
- Considering the variables available for measurement, in this case ω_r, $i_{\alpha s}$, and $i_{\beta s}$ are obtained after the Clark transformation (3) of the measured currents i_a, i_b and i_c, the estimation errors ϵ_1, ϵ_2, and ϵ_3 are created. These errors are used as information that helps the model (8) to achieve convergence.
- In the system described by Eq. (8), each equation includes terms $k_\bullet\ \mathrm{sign}(\epsilon_1)$ and $\alpha_\bullet\epsilon_1$. These terms arise because the angular speed is the primary variable to be controlled. Here, $\epsilon_1 = \omega_r - \hat{\omega}_r$ represents the error estimation for this variable. The term $k_\bullet\ \mathrm{sign}(\epsilon_1)$ incorporates a sign function to account for the direction of the error, while the term $\alpha_\bullet\epsilon_1$ directly influences the system dynamics.
- Regarding the equations for the variables $\hat{\lambda}_{\alpha r}$ and $\hat{i}_{\beta s}$, both equations include the term $k_\bullet\ \mathrm{sign}(\epsilon_2)$. This is due to system Eq. (7), in their corresponding equations, $\lambda_{\alpha r}$ and $i_{\beta s}$, both contain the term $i_{\alpha s}$. This term represents information about the error: $\epsilon_2 = i_{\alpha s} - \hat{i}_{\alpha s}$ for the estimated variables.
- Concerning the equations for the variables $\hat{\lambda}_{\beta r}$ and $\hat{i}_{\alpha s}$, both equations also feature the term $k_\bullet\ \mathrm{sign}(\epsilon_3)$. Again, this is due to system Eq. (7), in their corresponding equations, $\lambda_{\beta r}$ and $i_{\alpha s}$, both involve the term $i_{\beta s}$. Here, $i_{\beta s}$ provides information about the error: $\epsilon_3 = i_{\beta s} - \hat{i}_{\beta s}$ for the estimated variables.

Note that this is a particular methodology that the authors propose for estimating the non-linear system (7) with system (8) in the present proposal.

2.3.2. Robust observer for flux linkages

To make a comparison of the proposed sliding mode observer, a robust observer is used to estimate the variables $\lambda_{\alpha r}$ and $\lambda_{\beta r}$. Also, the asymptotic load torque observer is utilized. This is achieved by using the methodology proposed in an earlier work [23]. The procedure for obtaining the estimates of the variables $\lambda_{\alpha r}$ and $\lambda_{\beta r}$ consists of the following steps [23]:

- To represent the observer of the last four equations of system (7) in vector form as:

$$\begin{aligned}
\frac{d\hat{\boldsymbol{\lambda}}_r}{dt} &= \mathbf{A}_{11}\hat{\boldsymbol{\lambda}}_r + \mathbf{A}_{12}\hat{\mathbf{i}}_s - \mathbf{G}_1\mathbf{v}\\
\frac{d\hat{\mathbf{i}}_s}{dt} &= \mathbf{A}_{21}\hat{\boldsymbol{\lambda}}_r + \mathbf{A}_{22}\hat{\mathbf{i}}_s + \mathbf{B}_2\mathbf{v}_s + \mathbf{v}
\end{aligned} \tag{9}$$

  where $\hat{\boldsymbol{\lambda}}_r = \begin{bmatrix}\hat{\lambda}_{\alpha r} & \hat{\lambda}_{\beta r}\end{bmatrix}^\top$ is the rotor flux linkage vector estimator; $\hat{\mathbf{i}}_s = \begin{bmatrix}\hat{i}_{\alpha s} & \hat{i}_{\beta s}\end{bmatrix}^\top$ represents the estimator of the stator currents; $\mathbf{v}_s = \begin{bmatrix}v_{\alpha s} & v_{\beta s}\end{bmatrix}^\top$ is the input vector, $\mathbf{v} = \mathbf{N}\ \mathrm{sign}\left(\mathbf{i}_s - \hat{\mathbf{i}}_s\right)$, $\mathbf{N} = \begin{bmatrix}N_{11} & 0\\ 0 & N_{22}\end{bmatrix}$, and $\mathbf{G}_1 = \begin{bmatrix}G_{11} & 0\\ 0 & G_{22}\end{bmatrix}$. To check the remaining parameters, the reader is kindly referred to Ref. [23].
- To define the sliding manifold with the discontinuous function $\mathbf{v}$ such that the surface $\mathbf{s} = \boldsymbol{\epsilon}_{\mathbf{i}_s} = \mathbf{i}_s - \hat{\mathbf{i}}_s = 0$, which represents the estimation error vector of the stator currents. Besides, the estimation error vector of flux linkages $\boldsymbol{\epsilon}_{\lambda_r} = \lambda_r - \hat{\lambda}_r = 0$, this is done by choosing the correct positive values of the diagonal matrix $\mathbf{N}$, such that the sliding manifold $\mathbf{s}$ converges to zero in finite time.
- To involve the motor model (7) and the observer Eqs. (9) in order to determine the estimation error dynamics. Once the sliding manifold is achieved, the control input vector $\mathbf{v}$ of system (9) is the equivalent control v_{eq}.

For further details of the steps described above, the reader is kindly directed to Ref. [23].

2.3.3. Luenberger load torque observer

To make comparisons of the proposed sliding mode controller, the Luenberger Load torque observer, presented in [23], is used. This

is described as follows: taking the first equation of system (7), the equation for the angular speed estimator is:

$$\frac{d\hat{\omega}_r}{dt} = K_T\left(i_{\beta s}\hat{\lambda}_{\alpha r} - i_{\alpha s}\hat{\lambda}_{\beta r}\right) - \frac{B_m}{J_m}\hat{\omega}_r - \frac{1}{J_m}\hat{T}_L + l_1\left(\omega_r - \hat{\omega}_r\right) \tag{10}$$

and considering that the derivative of the load torque is zero, the estimation of the load torque is:

$$\frac{d\hat{T}_L}{dt} = l_2\left(\omega_r - \hat{\omega}_r\right) \tag{11}$$

where l_1 and l_2 of Eqs. (10) and (11), respectively, are the Luenberger gains. The procedure for adjusting them is explained in [23].

2.3.4. Sliding mode observer for load torque

The methodology for the sliding modes observer takes into account the first equation of the system (8) for estimating the angular speed as follows:

$$\frac{d\hat{\omega}_r}{dt} = K_T\left(\hat{i}_{\beta s}\hat{\lambda}_{\alpha r} - \hat{i}_{\alpha s}\hat{\lambda}_{\beta r}\right) - \frac{B_m}{J_m}\hat{\omega}_r - \frac{1}{J_m}\hat{T}_L + \alpha_1\epsilon_1 + k_1\ \text{sign}(\epsilon_1) \tag{12}$$

considering that the derivative of the load torque as $\hat{T}_L \approx 0$, the estimation of the load torque is:

$$\frac{d\hat{T}_L}{dt} = k_{10}\ \text{sign}\left(\epsilon_1\right) + \alpha_{10}\left(\epsilon_1\right) \tag{13}$$

where $\epsilon_1 = \omega_r - \hat{\omega}_r$.

2.4. Equivalent control algorithm

The control algorithm used in this work is the sliding mode, with the equivalent algorithm presented in our previous work [17]. This strategy consists of the following steps:

- To transform the non-linear system (7) to the block control form, based on the tracking error dynamics; which means that these new state variables are $\boldsymbol{\varepsilon}_1$ and $\boldsymbol{\varepsilon}_2$. The resulting transformation has the following general form:

$$\begin{aligned}\dot{\boldsymbol{\varepsilon}}_1 &= -\mathbf{K}_1\boldsymbol{\varepsilon}_1 + \mathbf{B}_1\left(\hat{\lambda}_r\right)\boldsymbol{\varepsilon}_2\\ \dot{\boldsymbol{\varepsilon}}_2 &= \mathbf{F}\left(\hat{\lambda}_r, \boldsymbol{\varepsilon}_1, \boldsymbol{\varepsilon}_2\right) - \mathbf{B}_2\mathbf{v}_s\\ \dot{\hat{\lambda}}_{\alpha r} &= F\left(\hat{\lambda}_{\alpha r}, \omega_{ref}, \varepsilon_\omega, \hat{\lambda}_{\beta r}, i_{\alpha s}\right)\end{aligned} \tag{14}$$

  where $\hat{\lambda}_r = \left[\hat{\lambda}_{\alpha s}\ \ \hat{\lambda}_{\beta s}\right]^\top$ is the rotor flux linkages vector estimator which feeds the block control form from system (8) and

$$\mathbf{v}_s = \left[v_{\alpha s}\ \ v_{\beta s}\right]^\top \tag{15}$$

  The new state variables are:

$$\boldsymbol{\varepsilon}_1 = \begin{bmatrix}\omega_{ref} - \omega_r\\ \phi_{ref} - \phi_r\end{bmatrix} \tag{16}$$

  and

$$\boldsymbol{\varepsilon}_2 = \left[\mathbf{i}_{ref} - \mathbf{i}_s\right] \tag{17}$$

  In this case $\phi_r = |\ \lambda_r| = \lambda_r^\top\lambda_r = \lambda_{\alpha r}^2 + \lambda_{\beta r}^2$ (in Wb^2) is the square modulus of the rotor flux linkages (the second variable to be controlled) with $\lambda_r = \left[\lambda_{\alpha s}\ \ \lambda_{\beta s}\right]^\top$, and ϕ_{ref} its reference signal. For simplicity, the complete procedure is not shown, and the reader is kindly referred to Refs. [17,23].
- The system (14) is used to design the sliding manifold $\mathbf{s}$, where this manifold is the equation of $\boldsymbol{\varepsilon}_2$. Then, the sliding surface is:

$$\mathbf{s} = \boldsymbol{\varepsilon}_2 \tag{18}$$

  and its dynamics is:

$$\dot{\mathbf{s}} = \mathbf{F}\left(\hat{\lambda}_r, \boldsymbol{\varepsilon}_1, \boldsymbol{\varepsilon}_2\right) - \mathbf{B}_2\mathbf{v}_s. \tag{19}$$

  Note that in this work, the equivalent control algorithm involves the estimated variable $\hat{\lambda}_{\alpha s}$ and $\hat{\lambda}_{\beta s}$ obtained from the system (8), also the external disturbance $\hat{T}_L$ (13). This is one of the main differences between this proposal and the one presented in [17].
- Once the sliding manifold is obtained, the control input $\mathbf{v}_s$ forces the of this manifold to zero in finite time, which means that the stator currents vector $\mathbf{i}_s$ tracks its reference signal $\mathbf{i}_{ref}$; additionally, the angular speed ω_r reaches its corresponding reference signal ω_{ref}, and also the squared rotor flux linkages ϕ_r tracks its corresponding reference signal ϕ_{ref}.

Given the mathematical model of the squirrel cage induction motor model (7), which the states $\lambda_{\alpha r}$ and $\lambda_{\beta r}$ are estimated with the states $\hat{\lambda}_{\alpha r}$ and $\hat{\lambda}_{\beta r}$ of system (8), and the load torque T_L is estimated with the sliding mode observer (13). The mathematical model (7) is transformed into the block control form (14) to design the sliding manifold such as the sliding mode with the equivalent control algorithm explained in Section 2.4 with the control input vector $\mathbf{v}_s = \left[v_{\alpha s}\ \ v_{\beta s}\right]^\top$ (15) forces the system of this manifold to zero in finite time, which means that the stator currents vector $\mathbf{i}_s$ tracks its reference signal $\mathbf{i}_{ref}$. Additionally, the angular speed ω_r reaches its corresponding reference signal ω_{ref}, and also the squared rotor flux linkages ϕ_r tracks its corresponding reference signal ϕ_{ref}. The stability analysis is given in Appendix B.

3. Evaluation of the proposed strategy

3.1. Design validation

In this work, three observers are used: sliding mode observer for rotor flux linkages and Load torque; asymptotic observer for flux linkages; and Luenberger observer for Load torque. The following tests are employed:

- Five different values of angular speed reference ω_{ref}, as shown in Table 2:
- Five different values in external disturbance T_L, as shown in Table 3 and illustrated in Fig. 5.
- A simulation is made with $\omega_{ref} = 500$ rev/min and with $T_L = 4$ N m, this is to analyze the root-mean-square (RMS) error.
- The reference signal for the rotor flux square modulus $\phi_{ref} = 0.21\ \text{Wb}^2$.
- The simulations are made in Simulink/Matlab™R2024a for a test duration of 1 s using the Runge–Kutta solver with a fixed-step size of 1×10^{-6} s. The parameters for the squirrel cage induction motor [16] are presented in Table 1.
- The obtained simulation results are:
  - Sliding mode observer (Smo) for estimating the variables $\hat{\lambda}_{\alpha r}$, $\hat{\lambda}_{\beta r}$, and $\hat{T}_L$.
  - Robust observer (Ro) for estimating the variables $\hat{\lambda}_{\alpha r}$ and $\hat{\lambda}_{\beta r}$.
  - Luenberger observer (Lo) for estimating the variable $\hat{T}_L$.
  - The angular speed tracking performance with the effect of Smo ($\hat{\lambda}_{\alpha r}$, $\hat{\lambda}_{\beta r}$, and $\hat{T}_L$), Ro ($\hat{\lambda}_{\alpha r}$ and $\hat{\lambda}_{\beta r}$), and Lo ($\hat{T}_L$).
  - Rotor flux square modulus tracking performance with the effect of Smo ($\hat{\lambda}_{\alpha r}$, $\hat{\lambda}_{\beta r}$, and $\hat{T}_L$), and Ro ($\hat{\lambda}_{\alpha r}$ and $\hat{\lambda}_{\beta r}$).

Table 2
Changes of angular speed reference ω_{ref}.

Time (s)	0	0.3	0.4	0.6	0.8
w_{ref} (rev/min)	500	700	300	600	550

Table 3
Changes of external disturbance T_L.

Time (s)	0	0.20	0.55	0.70	0.90
T_L (N m)	4	10	6	12	4

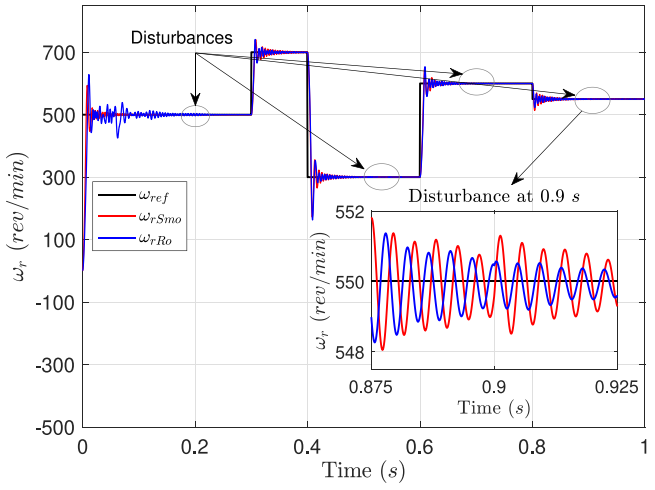

Fig. 2. Angular speed tracking performance.

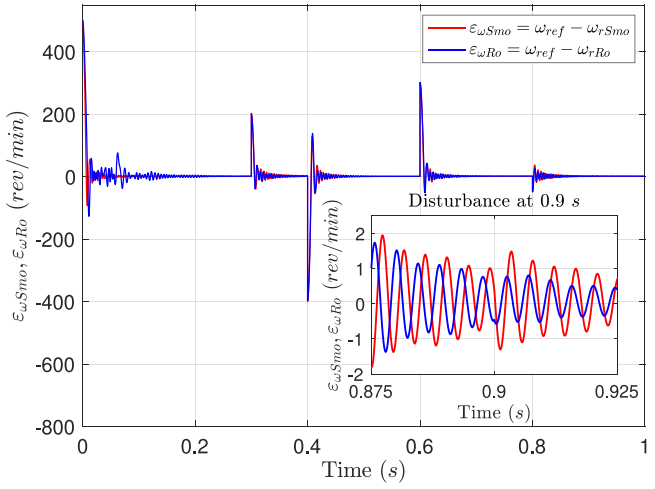

Fig. 3. Angular speed tracking performance errors $\varepsilon_{\omega Smo} = \omega_{ref} - \omega_{rSmo}$ and $\varepsilon_{\omega Ro} = \omega_{ref} - \omega_{rRo}$.

3.2. Simulation results

The simulation results are presented as follows:

- The angular speed tracking performance is illustrated in Fig. 2, where two observers are compared: the Sliding Mode Observer (SMO), which estimates $\hat{\lambda}_{\alpha r}$, $\hat{\lambda}_{\beta r}$, and $\hat{T}_L$, and the Robust Observer (Ro), which estimates $\hat{\lambda}_{\alpha r}$ and $\hat{\lambda}_{\beta r}$. The figure highlights the disturbances and transients resulting from changes in the angular speed reference, ω_{ref}. Additionally, it includes an expanded view focusing on the tracking and disturbance observed at 0.9 s. Notably, the enlarged detail before the disturbance reveals a diminishing oscillation, attributed to the transient response triggered by the change in angular speed reference from 600 to 550 rev/min at 0.8 s. It can also be seen that the amplitude of the oscillations using Ro is slightly higher compared to SMO. The tracking performance errors, $\varepsilon_{\omega_{\text{Smo}}} = \omega_{\text{ref}} - \omega_{r\text{Smo}}$ and $\varepsilon_{\omega_{\text{Ro}}} = \omega_{\text{ref}} - \omega_{r\text{Ro}}$, are depicted in Fig. 3, with an expanded detail at 0.9 s to emphasize the effect of the disturbance.
- The rotor flux square modulus tracking performance is depicted in Fig. 4. For this tracking, it was given a reference signal $\phi_{ref} = 0.21$ Wb^2. Note that the change in speed reference causes oscillation with greater amplitude than the disturbance changes. Also,

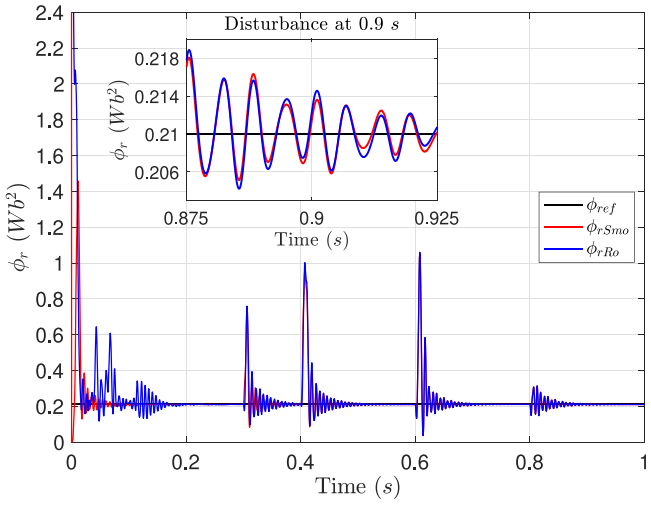

Fig. 4. Rotor flux square modulus tracking performance.

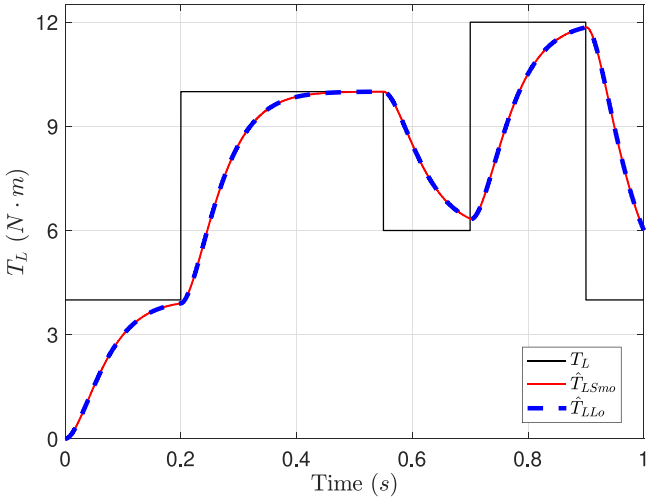

Fig. 5. Load Torque T_L estimation.

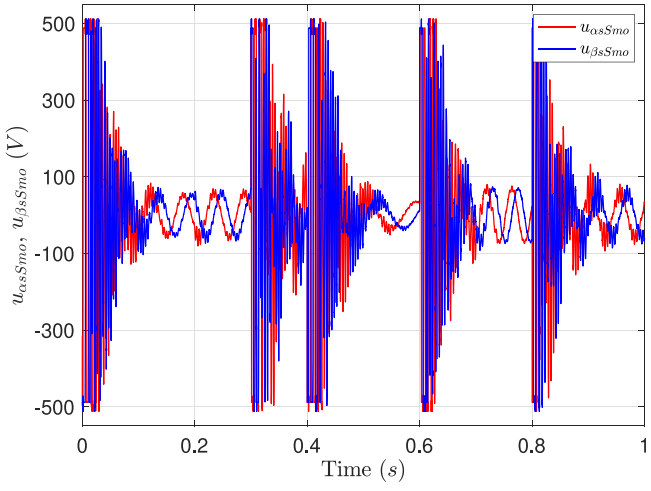

Fig. 6. Control input performance u_{as}, $u_{\beta s}$ using sliding mode observer.

an expansion detail is presented at 0.9 s of simulation for showing the behavior of this change of disturbance from 12 to 4 N m.

- In Fig. 5 is shown the estimation of the load torque T_L by using the values of Smo and Lo. Note that there is not much difference between these two estimators, and both have a rapid response to the disturbance. Note that this is a very short simulation time, and there is a fast response of the estimators, which implies that the estimators are effective.
- Figs. 6 and 7 present the control input signals performance using Smo ($u_{\alpha sSmo}$ and $u_{\beta sSmo}$) and Ro ($u_{\alpha sRo}$ and $u_{\beta sRo}$), respectively. Both figures show clearly that when there is a change of angular speed reference, the control signals the maximum amplitude voltage given by the source. Once the sliding modes are achieved, the equivalent control v_{eq} is applied. It is noted that when a change occurs in the angular speed reference ω_{ref}, the transient using the Smo is achieved faster than by using the Ro. This is due to the estimators of the Smo converging faster, too.
- In Figs. 8 and 9, the rotor flux linkages $\lambda_{\alpha rSmo}$ and $\lambda_{\beta rSmo}$, are shown. For both figures, the simulation results are presented for a period of 1 s (upper trace) and for 0.1 s (lower trace). In both cases, the convergence is very fast. Also, it can be seen that the change of angular speed reference ω_{ref} causes a little more oscillation than the change in external disturbance T_L. The flux linkages estimation errors $\epsilon_{\lambda_{\alpha rSmo}}$ (upper trace), and $\epsilon_{\lambda_{\beta rSmo}}$ (lower trace) are presented in Fig. 10. In this figure, the fast convergence of these estimators for both signals can also be observed.
- The same for Figs. 11 and 12 that are depicted the rotor flux linkages $\lambda_{\alpha Ro}$ and $\lambda_{\beta Ro}$, respectively, using Ro. Also, a simulation of 1 s (upper trace), and a detail of 0.1 s of the simulation (lower trace) are shown. It was noted that convergence is not achieved as fast as using Smo. Also, the changes in angular speed reference cause more oscillations than the load torque change. Additionally, the flux linkages estimation errors $\epsilon_{\lambda_{\alpha Ro}}$ (upper trace), and $\epsilon_{\lambda_{\beta Ro}}$ (lower trace) are displayed in Fig. 13. This figure shows the transient of the convergence for the two signals.
- To assess the accuracy of the estimation process for steady-state $\lambda_{\alpha r}$, $\lambda_{\beta r}$, T_L, and its impact on angular speed tracking, we include an analysis that focuses on three key metrics: Root Mean Square (RMS), Integral of Absolute Error (IAE), and Integral of Squared Error (ISE). These metrics are essential for understanding how well each observer tracks or estimates the variables. This analysis is provided in Table 4 and complemented with Fig. 14. The figure and table provide a comparison of the performance of three different observers: the Sliding Mode Observer (Smo), the Robust Observer (Ro), and the Luenberger Observer (Lo). The variables analyzed are the angular speed ω_r, the flux linkages $\lambda_{\alpha r}$, $\lambda_{\beta r}$, and the load torque T_L. The analysis is explained as follows:

1. Tracking of angular speed ω_r

From Fig. 14a and Table 4, we observe the following for the tracking of ω_r:

- **RMS:** Using Smo observer, the result has a lower RMS error (0.0040 rpm) compared to Ro (0.0117 rpm), indicating better stability and lower error for angular speed tracking.
- **IAE:** The IAE, for angular speed tracking, shows that Smo (0.0393 rev) performs slightly better than Ro (0.0521 rev) in terms of accumulated absolute error.
- **ISE:** The ISE, further highlights that Smo (0.0030 rev^2) outperforms Ro (0.0088 rev^2), confirming Smo's better overall performance in reducing cumulative squared errors for angular speed tracking.

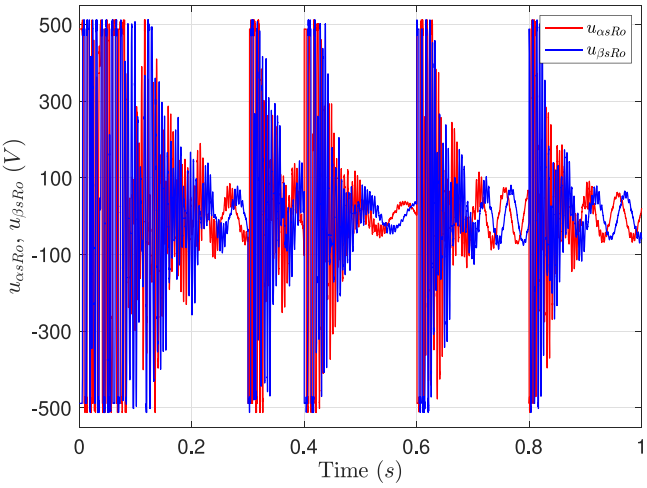

Fig. 7. Control input performance u_α, u_β using Robust observer.

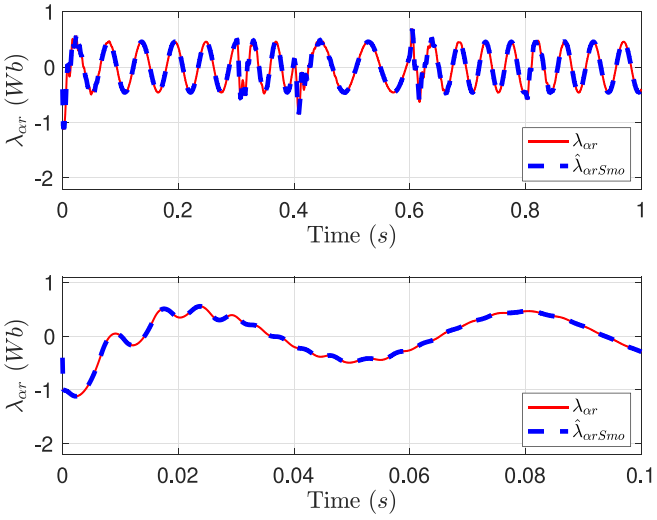

Fig. 8. Rotor flux linkages $\lambda_{\alpha r}$ using sliding mode observer.

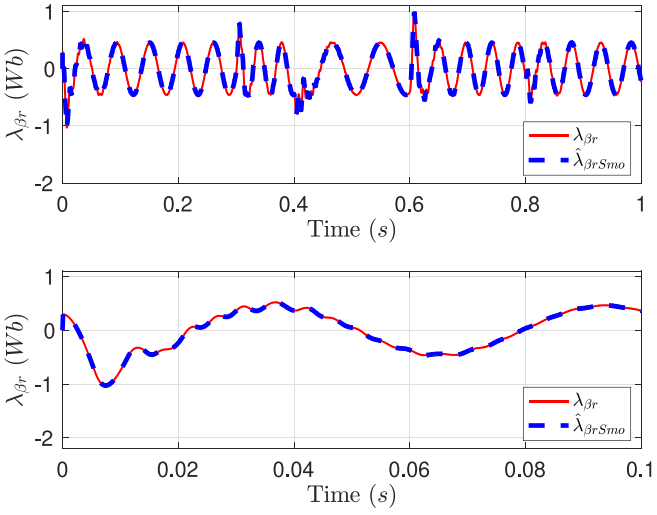

Fig. 9. Rotor flux linkages $\lambda_{\beta r}$ using sliding mode observer.

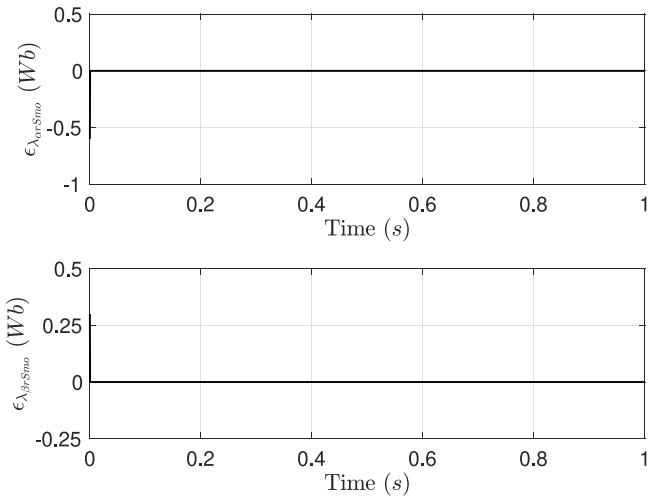

Fig. 10. Flux linkages estimation errors $\epsilon_{\lambda_{arSmo}}$ (upper trace), and $\epsilon_{\lambda_{\beta rSmo}}$ (lower trace) using sliding mode observer.

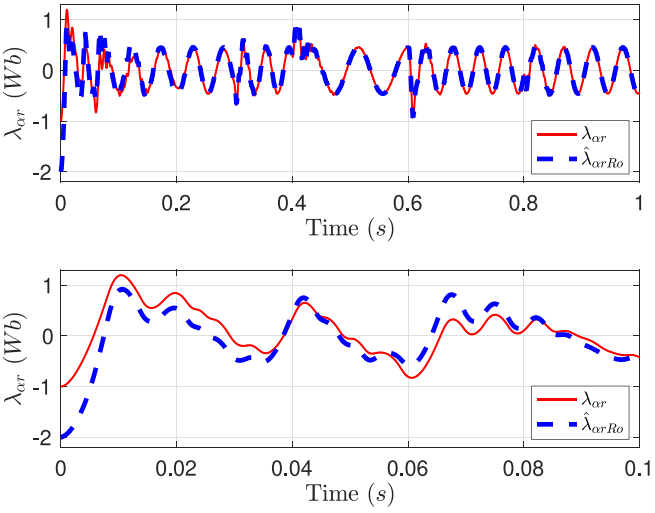

Fig. 11. Rotor flux linkages $\lambda_{\alpha r}$ using Luenberger observer.

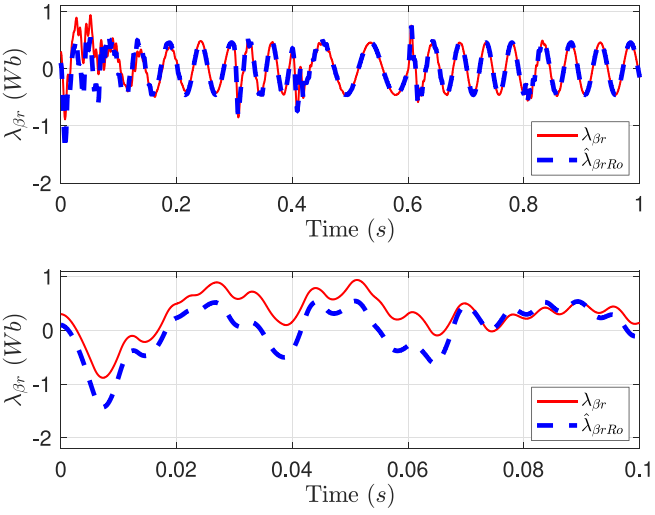

Fig. 12. Rotor flux linkages $\lambda_{\beta r}$ using Luenberger observer.

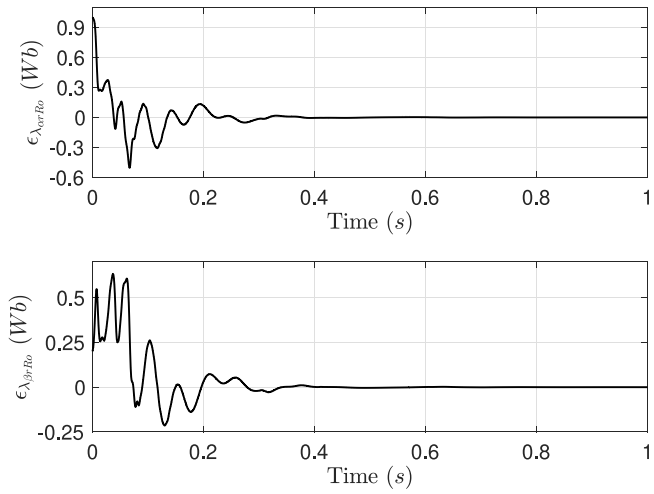

Fig. 13. Flux linkages estimation errors $\epsilon_{\lambda_{\alpha rRo}}$ (upper trace), and $\epsilon_{\lambda_{\beta rRo}}$ (lower trace) using Luenberger observer.

2. Estimation of flux linkages $\lambda_{\alpha r}$

Fig. 14(b) and Table 4 compare the performance for estimating $\lambda_{\alpha r}$:

- **RMS:** Ro provides much better performance with a significantly lower RMS error (0.0125 Wb) compared to Smo (0.1001 Wb).
- **IAE:** In terms of accumulated absolute error, Smo (0.0016 Wb s) outperforms Ro (0.0380 Wb s).
- **ISE:** For squared error, Ro (0.0125 Wb^2 s) performs significantly better than Smo (0.0930 Wb^2 s), indicating greater stability for Ro.

3. Estimation of flux linkages $\lambda_{\beta r}$

From Fig. 14(c) and Table 4, the estimation of $\lambda_{\beta r}$ is analyzed:

- **RMS:** Smo shows better RMS performance with a lower error (0.0634 Wb) compared to Ro (0.0147 Wb).
- **IAE:** The IAE for Smo (0.4004 Wb s) is slightly smaller than Ro (0.4420 Wb s).
- **ISE:** Smo also provides a better ISE value (0.0589 Wb^2 s) than Ro (0.0147 Wb^2 s).

4. Estimation of load torque T_L

Fig. 14(d), the estimation of load torque T_L is analyzed:

- **RMS:** Both Smo (0.0026 N m) and Ro (0.0028 N m) show similar performance in terms of RMS error.
- **IAE:** The accumulated absolute error for Smo (0.0129 N m s) and Ro (0.0134 N m s) is quite similar.
- **ISE:** Smo (0.0022 $(N\,m)^2$ s) performs slightly better than Ro (0.0024 $(N\,m)^2$ s) for the squared error analysis.

Overall analysis

- For angular speed tracking (ω_r), the Smo observer performs better in IAE and ISE, while Ro shows a slightly higher RMS error.
- In the estimation of flux linkages $\lambda_{\alpha r}$ and $\lambda_{\beta r}$, Ro generally provides better performance, especially in RMS and ISE values. However, Smo outperforms Ro in terms of the IAE for $\lambda_{\alpha r}$.
- For load torque estimation (T_L), Smo and Ro have similar performances across all metrics, with Smo slightly outperforming Ro in the ISE metric.

Table 4
Comparison of RMS, IAE, and ISE of the Angular speed ω_r tracking, λ_{ar}, $\lambda_{\beta r}$, and Load torque T_L estimation using sliding modes (Smo), Robust (Ro), and Luenberger (Lo) observers.

Observer	Variable analysis	ω_r Tracking	λ_{ar} Estimation	$\lambda_{\beta r}$ Estimation	T_L Estimation
Smo	RMS	0.0040 rpm	0.1001 Wb	0.0634 Wb	0.0026 N m
	IAE	0.0393 rev	0.0016 Wb s	0.4004 Wb s	0.0129 N m s
	ISE	0.0030 rev^2	0.0930 Wb^2 s	0.0589 Wb^2 s	0.0022 (Nm)^2 s
Ro	RMS	0.0117 rpm	0.0125 Wb	0.0147 Wb	–
	IAE	0.0521 rev	0.0380 Wb s	0.4420 Wb s	–
	ISE	0.0088 rev^2	0.0125 Wb^2 s	0.0147 Wb^2 s	–
Lo	RMS	–	–	–	0.0028 Nm
	IAE	–	–	–	0.0134 Nm s
	ISE	–	–	–	0.0024 (N m)^2 s

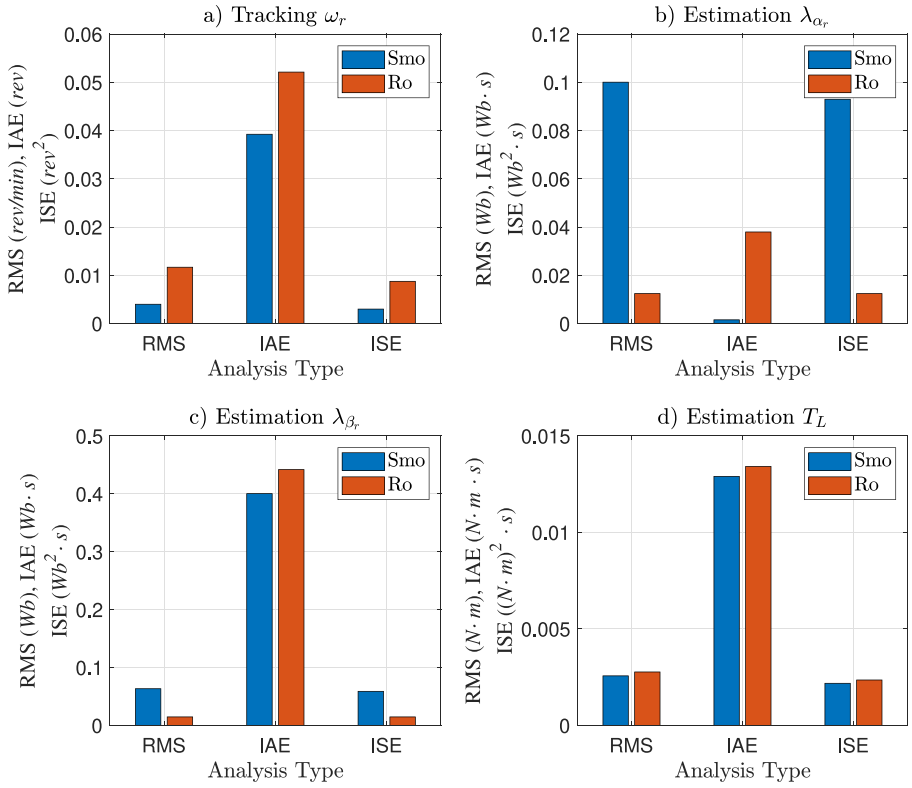

Fig. 14. Comparison of MSE, IAE, and ISE of the errors of (a) angular speed tracking ω_r, estimation of (b) λ_{ar}, (c) $\lambda_{\beta r}$, and (d) T_L.

Table 5
Angular speed tracking accuracy using RMS, IAE, and ISE analysis.

Metric	RMS accuracy (%)	IAE accuracy (%)	ISE accuracy (%)
Smo	97.5%	96.8%	95.3%
Ro	94.2%	93.5%	92.1%

Table 5 presents a detailed comparison of the angular speed tracking accuracy achieved using two different observers: the Sliding Mode Observer (Smo) and the Robust Observer (Ro). The Smo estimates $\hat{\lambda}_{ar}$, $\hat{\lambda}_{\beta r}$, and $\hat{T}_L$, while the Ro estimates only $\hat{\lambda}_{ar}$ and $\hat{\lambda}_{\beta r}$. The underlying control strategy employed is based on sliding modes, incorporating an equivalent control algorithm to ensure accurate speed tracking. To assess the angular speed tracking performance with the effect of each observer, three key metrics — RMS (Root Mean Square), IAE (Integral of Absolute Error), and ISE (Integral of Squared Error) — were used. These metrics provide a comprehensive evaluation of how effectively each observer tracks the desired angular speed, highlighting their precision, consistency, and sensitivity to deviations. The explanation of the results is given next:

- **Smo (Sliding Mode Observer):**
  - **RMS Accuracy (97.5%):** Smo achieves a very high accuracy level, indicating excellent average performance in maintaining the desired speed.
  - **IAE Accuracy (96.8%):** Reflects that Smo effectively minimizes deviations, with a consistent level of precision over time.
  - **ISE Accuracy (95.3%):** Shows slightly lower accuracy compared to RMS and IAE, indicating a minor sensitivity to occasional larger deviations.
- **Ro (Robust Observer):**
  - **RMS Accuracy (94.2%):** Slightly lower than Smo, suggesting that Ro's average performance is good but not as precise.
  - **IAE Accuracy (93.5%):** Indicates that Ro permits more accumulated errors over time, resulting in a slightly reduced precision.
  - **ISE Accuracy (92.1%):** The lowest among the metrics, showing that Ro may be more sensitive to occasional larger deviations compared to Smo.

Table 6
Comparison of the results obtained in this proposal with some similar works in the literature.

Issue	Reference	Present Proposal	Observations
Angular speed tracking error	[17] 0.1797 rpm. Do not use observers	0.0040 rpm	Both use similar conditions, control algorithm, and the same electrical machine.
Accuracy	[10] ±0.02 rad/s p.u ±0.009 rad/s p.u. reduced	97.5% RMS 96.8% IAE 95.3% ISE	Reference [10] uses ST-SMO This work uses Smo
Accuracy	[8] 97.33%	97.5% RMS 96.8% IAE 95.3% ISE	Reference [8] uses ISMC This work uses Smo
Tracking performance	[3] Slight advantage, Percentages are not given	0.004 rpm RMS 0.0393 rev IAE 0.0030 rev^2 ISE	Reference [3] uses FTSMO This work uses Smo Difficult to compare quantitatively
Estimation errors	[3] Rotor speed and position estimation errors are significantly lower with FTSMO	0.004 rpm RMS 0.0393 rev IAE 0.0030 rev^2 ISE	Reference [3] estimates rotor speed and position This work does not

The table provides a clear comparison between the two observers, demonstrating that Smo achieves higher accuracy across all metrics, making it more effective for precise speed tracking. Although Ro also performs well, its slightly lower accuracy percentages suggest that it may not be as consistent or precise, especially when dealing with larger tracking errors. In general, the accuracy values presented here help to evaluate which observer better maintains the desired motor speed under different conditions. High percentages across all three metrics indicate a reliable and precise control performance.

4. Conclusion

In this paper, the effectiveness of a high-precision EMDS utilizing an 84-pulse VSC for the speed control of induction motors was demonstrated through extensive simulations conducted in a Matlab/Simulink environment. The key parameters for developing the VSC signal, V_{module}, and the variable frequency adjusted via a PLL, proved crucial in achieving precise modulation of 3-phase signals.

The integration of sliding-mode, asymptotic, and Luenberger observers for estimating non-measurable variables significantly enhanced the system's robustness and accuracy. The control algorithm based on sliding modes with an equivalent control strategy showed excellent performance, maintaining stability and precision across various operating conditions. This approach effectively managed uncertainties and disturbances, ensuring reliable motor control.

Overall, the combination of an 84-pulse VSC, advanced observer-based estimation techniques, and a sliding-mode control strategy constitutes a powerful framework for high-performance induction motor drives, paving the way for further advancements in motor control technology.

5. Discussion

It is important to emphasize that a key contribution of this work is the development of the sliding mode observer, as formulated in system (8), which is based on the specific methodology outlined in detail in Section 2.3.1. Furthermore, the sliding mode observer for load torque, presented in Eqs. (13) and discussed in Section 2.3.4, represents another major innovation in this study. Finally, the validation of these observers and the sliding mode with an equivalent control algorithm is conducted via an extensive set of simulations applied to the squirrel cage induction motor model using the 84-pulse VSC.

When applied to the squirrel cage induction motor, where flux linkages $\lambda_{\alpha r}$ and $\lambda_{\beta r}$, as well as load torque T_L, are estimated using a sliding mode observer, the chattering effect is significantly mitigated. The main reason behind this reduction in chattering is the transformation of the system into a control-friendly form that allows for smoother control actions. This is particularly crucial for the squirrel cage induction motor, where chattering could otherwise result in unwanted high-frequency oscillations, leading to mechanical wear, noise, and efficiency losses. In the context of the sliding mode observer, the estimation of the flux linkages $\lambda_{\alpha r}$ and $\lambda_{\beta r}$, and the load torque T_L complements the Equivalent Control Algorithm by providing accurate state information, which helps in applying more refined control inputs. As a result, the combined use of Utkin's algorithm [1,2] and Loukianov's block control form [14] permits robust performance while minimizing the harmful effects of chattering, improving the overall stability and efficiency of the induction motor system.

The results obtained by this proposal have been compared with others reported in the literature. The RMS value of the angular speed tracking error reported in [17] is 0.1797 rpm, while the one reported in this work is 0.0040 rpm. This comparison is performed using similar conditions, such as a control algorithm and the same electrical machine, but the Ref. [17] does not use observers. On the other hand, the work presented in [10], does not directly provide specific numerical values or percentages for the accuracy of tracking and estimation processes. However, it mentions that the proposed Super-Twisting Sliding Mode Observer (ST-SMO) maintains the motor's inaccuracy within ±0.02 rad/s per unit (p.u) due to load disturbances, which can be reduced to ±0.009 rad/s p.u after some recovery. Then, it would be better to have more statistical results to compare this reference with our proposal. In the case of the article [3], the proposed FTSMO shows a slight advantage in tracking performance over the conventional sliding mode observer (SMO). While exact percentages are not given, the text indicates that the tracking error is reduced, suggesting an improvement in accuracy. With regards to estimation errors, the authors report that the rotor-speed estimation and position estimation errors are described as significantly lower with the FTSMO. estimation processes. In summary, while the document does not specify exact percentages, it indicates that the FTSMO provides a notable improvement in accuracy over traditional methods, which could be quantified with further detailed simulation results or experimental validation. In the study conducted by [8], the authors demonstrate that the Integral Sliding Mode Controller (ISMC) achieves a 97.33% reduction in steady-state error compared to a traditional PI controller. When comparing these results to the proposed method, Table 5 indicates that the accuracy achieved using the Sliding Mode Observer (SMO) is 97.5% based on the RMS analysis. This suggests that the performance of the SMO slightly exceeds that of the ISMC reported by [8], highlighting the effectiveness of our control strategy. Table 6 provides a summary comparing the results obtained in this study with those previously discussed. This comparison highlights the performance and key differences, offering a clear perspective on the contributions and advancements presented in this work relative to the existing solutions.

CRediT authorship contribution statement

Carlos E. Castañeda: Writing – review & editing, Writing – original draft, Validation, Software, Methodology, Formal analysis, Conceptualization. **Antonio Valderrabano-Gonzalez:** Writing – review & editing, Writing – original draft, Supervision, Software, Project administration, Methodology, Funding acquisition, Conceptualization. **Hossam A. Gabbar:** Writing – review & editing, Validation, Supervision, Project administration. **Vijay K. Sood:** Writing – review & editing, Validation, Supervision, Methodology.

Funding

This work was supported by Universidad Panamericana through the Fondo Fomento a la Investigación UP 2024 under Project UP-CI-2024-GDL-10-ING.

Declaration of competing interest

The authors declare that they have no known competing financial interests or personal relationships that could have appeared to influence the work reported in this paper.

Acknowledgments

The authors gratefully acknowledge the support of Universidad Panamericana Campus Guadalajara and Centro Universitario de los Lagos of the Universidad de Guadalajara.

Appendix A. Convergence estimator analysis

The convergence of the observer (8) is presented by defining the state vector of the system (7) as $\mathbf{x} = \left[x_1\ x_2\ x_3\ x_4\ x_5\right]^\top = \left[\omega_r\ \lambda_{\alpha r}\ \lambda_{\beta r}\ i_{\alpha s}\ i_{\beta s}\right]^\top$, and the one of system (8) as $\hat{\mathbf{x}} = \left[\hat{x}_1\ \hat{x}_2\ \hat{x}_3\ \hat{x}_4\ \hat{x}_5\right]^\top = \left[\hat{\omega}_r\ \hat{\lambda}_{\alpha r}\ \hat{\lambda}_{\beta r}\ \hat{i}_{\alpha s}\ \hat{i}_{\beta s}\right]^\top$; the estimation error vector is $\hat{\epsilon} = \mathbf{x} - \hat{\mathbf{x}}$, with dynamics:

$$\begin{aligned}\dot{\hat{\epsilon}} =& \dot{\mathbf{x}} - \dot{\hat{\mathbf{x}}} \\ =& -\boldsymbol{\alpha}_1\boldsymbol{\epsilon}_1 - \mathbf{K}_1\ \mathbf{sign}\left(\boldsymbol{\epsilon}_1\right) - \boldsymbol{\alpha}_2\boldsymbol{\epsilon}_2 - \mathbf{K}_2\ \mathbf{sign}\left(\boldsymbol{\epsilon}_2\right)\end{aligned} \tag{A.1}$$

Let $\boldsymbol{\alpha}_1$ be an $n \times n$ diagonal matrix with $n = 5$, having constant positive diagonal elements $\alpha_1, \alpha_2, \ldots, \alpha_5$. Similarly, let $\boldsymbol{\epsilon}_1$ denote a 5×1 vector with components ϵ_1. The matrix $\mathbf{K}_1$ is also an $n \times n$ diagonal matrix, with constant positive diagonal values $k_1, k_2, \ldots, k_5$. The vector $\mathbf{sign}(\boldsymbol{\epsilon}_1)$ is a 5×1 vector with elements $\mathrm{sign}(\epsilon_1)$.

Next, let $\boldsymbol{\alpha}_2$ be an $(n-1) \times (n-1)$ diagonal matrix, with constant positive diagonal elements $\alpha_6, \alpha_7, \ldots, \alpha_9$. The vector $\boldsymbol{\epsilon}_2$ is a 4×1 vector given by $\left[\epsilon_2\ \epsilon_3\ \epsilon_2\ \epsilon_3\right]^\top$, and $\mathbf{K}_2$ is an $(n-1) \times (n-1)$ diagonal matrix with constant positive diagonal elements $k_6, k_7, \ldots, k_9$. The vector $\mathbf{sign}(\boldsymbol{\epsilon}_2)$ is a 4×1 vector given by $\left[\mathrm{sign}(\epsilon_2)\ \mathrm{sign}(\epsilon_3)\ \mathrm{sign}(\epsilon_2)\ \mathrm{sign}(\epsilon_3)\right]^\top$.

Note that to ensure the correct dimensions for matrices $\boldsymbol{\alpha}_2$ and $\mathbf{K}_2$, two vectors of dimensions $[0]_{1\times5}$ and $[0]_{4\times1}$ have been added to the first row and column, respectively. These additions do not affect the analysis of convergence. Similarly, for the vectors $\boldsymbol{\epsilon}_2$ and $\mathbf{sign}(\boldsymbol{\epsilon}_2)$, an additional scalar $[0]_{1\times1}$ has been incorporated.

It is evident that the values of the matrices $\boldsymbol{\alpha}_1$, $\boldsymbol{\alpha}_2$ $\mathbf{K}_1$, and $\mathbf{K}_2$ have been carefully selected to ensure that their eigenvalues are located at the desired locations in the left half of the complex plane.

We aim to demonstrate the convergence of the estimation variables of the system characterized by matrices $\boldsymbol{\alpha}_1$, $\boldsymbol{\alpha}_2$ $\mathbf{K}_1$, and $\mathbf{K}_2$, whose eigenvalues are carefully positioned in the left half of the complex plane. Let λ_i denotes the eigenvalues of these matrices. The convergence can be assured by considering a Lyapunov function $V(x)$ defined as $V(x) = x^\top P x$, where x represents the state vector. By selecting P such that it satisfies the Lyapunov equation $A^\top P + PA < 0$ for the system matrix A, we ensure that $V(x)$ is positive definite and its derivative $\dot{V}(x)$ is negative definite. This implies that $V(x)$ decreases over time, indicating asymptotic convergence.

The placement of eigenvalues in the left half of the complex plane ensures that the estimation error vectors $\boldsymbol{\epsilon}_1$, and $\boldsymbol{\epsilon}_2$ converge to zero in finite time. Specifically, the selection of $\boldsymbol{\alpha}_1$, $\boldsymbol{\alpha}_2$ $\mathbf{K}_1$, and $\mathbf{K}_2$ ensures that their collective influence maintains convergence conditions according to Lyapunov's criteria. Therefore, despite potential variations or disturbances, the system remains stable under operating conditions, validating the robustness and reliability of the chosen eigenvalue placement strategy. ■

Appendix B. Stability analysis using Lyapunov methodology

The stability of the sliding manifold (18) and the closed-loop system of the form (14) is analyzed using the Lyapunov methodology. For this, the Lyapunov function is chosen as follows:

$$V(\boldsymbol{\epsilon}_1, \boldsymbol{\epsilon}_2) = \frac{1}{2}\boldsymbol{\epsilon}_1^\top \mathbf{P}_1 \boldsymbol{\epsilon}_1 + \frac{1}{2}\boldsymbol{\epsilon}_2^\top \mathbf{P}_2 \boldsymbol{\epsilon}_2 \tag{B.1}$$

where $\boldsymbol{\epsilon}_1$ (16) and $\boldsymbol{\epsilon}_2$ (17) are the tracking errors, and $\mathbf{P}_1$ and $\mathbf{P}_2$ are positive definite matrices chosen such that it is possible to guarantee stability. The time derivative of the Lyapunov function (B.1) is:

$$\dot{V}(\boldsymbol{\epsilon}_1, \boldsymbol{\epsilon}_2) = \boldsymbol{\epsilon}_1^\top \mathbf{P}_1 \dot{\boldsymbol{\epsilon}}_1 + \boldsymbol{\epsilon}_2^\top \mathbf{P}_2 \dot{\boldsymbol{\epsilon}}_2 \tag{B.2}$$

Now, substituting the dynamic errors $\dot{\boldsymbol{\epsilon}}_1$ and $\dot{\boldsymbol{\epsilon}}_2$ from the block control form (14) in Eq. (B.2), we obtain:

$$\dot{V}(\boldsymbol{\epsilon}_1, \boldsymbol{\epsilon}_2) = -\boldsymbol{\epsilon}_1^\top \mathbf{P}_1 \mathbf{K}_1 \boldsymbol{\epsilon}_1 + \boldsymbol{\epsilon}_1^\top \mathbf{P}_1 \mathbf{B}_1(\hat{\lambda}_r)\boldsymbol{\epsilon}_2 + \boldsymbol{\epsilon}_2^\top \mathbf{P}_2 \mathbf{F}(\hat{\lambda}_r, \boldsymbol{\epsilon}_1, \boldsymbol{\epsilon}_2) - \boldsymbol{\epsilon}_2^\top \mathbf{P}_2 \mathbf{B}_2 \mathbf{v}_s \tag{B.3}$$

The control input $\mathbf{v}_s$ (15) is designed to force the sliding surface $\mathbf{s}$ (18) to zero in finite time. Specifically, we use the equivalent control method, where the control law from (14) is:

$$\mathbf{v}_s = \mathbf{B}_2^{-1}\left(\mathbf{F}(\hat{\lambda}_r, \boldsymbol{\epsilon}_1, \boldsymbol{\epsilon}_2) + k_s\ \mathrm{sign}(\mathbf{s})\right) \tag{B.4}$$

where k_s is a positive constant. Substituting this control law (B.4) into the Lyapunov derivative (B.3) yields:

$$\dot{V} = -\boldsymbol{\epsilon}_1^\top \mathbf{P}_1 \mathbf{K}_1 \boldsymbol{\epsilon}_1 - k_s \|\boldsymbol{\epsilon}_2\| \tag{B.5}$$

Since both terms are negative definite, $\dot{V}$ (B.5) is negative definite, ensuring that the errors $\boldsymbol{\epsilon}_1$ and $\boldsymbol{\epsilon}_2$ converge to zero in finite time. Thus, the sliding manifold (18) is reached in finite time, and the stator currents $\mathbf{i}_s$ track their reference signals $\mathbf{i}_{ref}$, the rotor speed ω_r reaches its reference ω_{ref}, and the rotor flux linkages ϕ_r track their reference ϕ_{ref}. This completes the stability proof using the Lyapunov methodology. ■

Data availability

No data was used for the research described in the article.

References

[1] Vadim Utkin, Jürgen Guldner, Jingxin Shi, Sliding Mode Control in Electro-Mechanical Systems, CRC Press, 2017.
[2] Vadim I. Utkin, Alex S. Poznyak, Adaptive sliding mode control with application to super-twist algorithm: Equivalent control method, Automatica 49 (1) (2013) 39–47.
[3] Vahid Teymoori, Hossein Dastres, Maarten J Kamper, Rong-Jie Wang, Nima Arish, Enhanced fast terminal sliding mode observer for wide-speed sensorless control of PM vernier ship propulsion machine drives, in: 2023 International Aegean Conference on Electrical Machines and Power Electronics (ACEMP) & 2023 International Conference on Optimization of Electrical and Electronic Equipment (OPTIM), IEEE, 2023, pp. 1–7.
[4] Bo Wang, Yanzhen Shao, Yong Yu, Qinghua Dong, Zhipeng Yun, Dianguo Xu, High-order terminal sliding-mode observer for chattering suppression and finite-time convergence in sensorless SPMSM drives, IEEE Trans. Power Electron. 36 (10) (2021) 11910–11920.
[5] Onofre A Morfin, Riemann Ruiz-Cruz, Fredy A Valenzuela, Reymundo Ramirez-Betancour, Carlos E Castañeda, Fernando Ornelas-Tellez, Robust cascade controller for the power factor of the three-phase supply and the induction motor velocity, ISA Trans. 140 (2023) 472–482.

[6] Ton Hoang Nguyen, Ty Trung Nguyen, Vinh Quang Nguyen, Kien Minh Le, Hoang Ngoc Tran, Jae Wook Jeon, An adaptive sliding-mode controller with a modified reduced-order proportional integral observer for speed regulation of a permanent magnet synchronous motor, IEEE Trans. Ind. Electron. 69 (7) (2021) 7181–7191.
[7] Tianqing Wang, Bo Wang, Yong Yu, Dianguo Xu, High-order sliding-mode observer with adaptive gain for sensorless induction motor drives in the wide-speed range, IEEE Trans. Ind. Electron. 70 (11) (2022) 11055–11066.
[8] Samar Abdulkareem AL-Hashemi, AL-Dujaili Ayad, Ahmed R. Ajel, Speed control using an integral sliding mode controller for a three-phase induction motor, J. Tech. 3 (3) (2021) 10–19.
[9] Xueqian Cao, Qiongxuan Ge, Jinquan Zhu, Ganlin Kong, Bo Zhang, Xiaoxin Wang, Improved sliding mode traction control combined sliding mode disturbance observer strategy for high-speed maglev train, IEEE Trans. Power Electron. 38 (1) (2022) 827–838.
[10] Lelisa Wogi, Marcin Morawiec, Tadele Ayana, Sensorless control of induction motor based on super-twisting sliding mode observer with speed convergence improvement, IEEE Access (2024).
[11] Salah Laghrouche, Fayez Shakil Ahmed, Adeel Mehmood, Pressure and friction observer-based backstepping control for a VGT pneumatic actuator, IEEE Trans. Control Syst. Technol. 22 (2) (2013) 456–467.
[12] Tao Jing, Alexander S. Maklakov, A review of voltage source converters for energy applications, in: 2018 International Ural Conference on Green Energy (UralCon), 2018, pp. 275–281.
[13] Francisco Beltran-Carbajal, Ruben Tapia-Olvera, Antonio Valderrabano-Gonzalez, Irvin Lopez-Garcia, Adaptive neuronal induction motor control with an 84-pulse voltage source converter, Asian J. Control (2020).
[14] Loukianov Alexander, et al., Robust block decomposition sliding mode control design, Math. Probl. Eng. 8 (4–5) (2003) 349–365.
[15] Colm J O'Rourke, Mohammad M Qasim, Matthew R Overlin, James L Kirtley, A geometric interpretation of reference frames and transformations: dq0, Clarke, and Park, IEEE Trans. Energy Convers. 34 (4) (2019) 2070–2083.
[16] Paul Krause, Oleg Wasynczuk, Scott D. Sudhoff, Steven Pekarek, Symmetrical induction machines, in: Analysis of Electric Machinery and Drive Systems, third ed., Wiley–IEEE Press, New Jersey, USA, 2013, pp. 244–245.
[17] Carlos E Castañeda, Antonio Valderrabano-Gonzalez, Hossam A Gabbar, Onofre A Morfín, Sliding mode with equivalent control for induction motor drive based on multi-pulse VSC, Energies 16 (13) (2023) 4866.
[18] Antonio Valderrabano-Gonzalez, F Beltran-Carbajal, R Tapia-Olvera, O Aguilar-Mejia, JC Rosas-Caro, Design methodology for interfacing DERs to power systems through VSC, Math. Probl. Eng. 2021 (2021) 1–10.
[19] Antonio Valderrabano, Juan M. Ramirez, A novel voltage source converter behind the StatCom, Electr. Power Compon. Syst. 38 (10) (2010) 1161–1174.
[20] F Beltran-Carbajal, R Tapia-Olvera, A Valderrabano-Gonzalez, H Yanez-Badillo, JC Rosas-Caro, JC Mayo-Maldonado, Closed-loop online harmonic vibration estimation in DC electric motor systems, Appl. Math. Model. 94 (2021) 460–481.
[21] Francisco Beltran-Carbajal, Ruben Tapia-Olvera, Antonio Valderrabano-Gonzalez, Irvin Lopez-Garcia, Adaptive neuronal induction motor control with an 84-pulse voltage source converter, Asian J. Control 23 (4) (2021) 1603–1616.
[22] Antonio Valderrabano-Gonzalez, Juan M. Ramirez, Ruben Tapia-Olvera, Julio C. Rosas-Caro, Jose M. Lozano-Garcia, Juan Miguel Gonzalez-Lopez, Analysis and implementation of an 84-pulse STATCOM, in: Farhad Shahnia, Sumedha Rajakaruna, Arindam Ghosh (Eds.), Static Compensators (STATCOMs) in Power Systems, Springer Singapore, Singapore, 2015, pp. 83–110.
[23] Onofre A Morfin, Fredy Alberto Valenzuela, Reymundo Ramírez Betancour, Carlos Eduardo CastañEda, Riemann Ruiz-Cruz, Antonio Valderrabano-Gonzalez, Real-time SOSM super-twisting combined with block control for regulating induction motor velocity, IEEE Access 6 (2018) 25898–25907.
[24] Onofre A Morfín, Carlos E Castañeda, Riemann Ruiz-Cruz, Fredy A Valenzuela, Miguel A Murillo, Abel E Quezada, Nahitt Padilla, The squirrel-cage induction motor model and its parameter identification via steady and dynamic tests, Electr. Power Compon. Syst. 46 (3) (2018) 302–315.

Dr. Carlos Eduardo Castañeda. Received the B.S. degree in communications and electronics from the Universidad de Guadalajara Mexico, in 1995, the M.Sc. degree in electronics and computer systems from the Universidad la Salle Bajío Mexico, in 2003, and the Ph.D. degree in electrical engineering from CINVESTAV Guadalajara, México, in 2009. He is a Professor with the Centro Universitario de los Lagos, Universidad de Guadalajara, México. His research interests include automatic control and renewable energy sources.

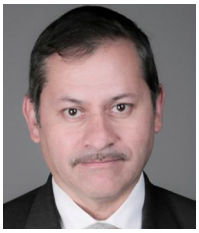

Dr. Antonio Valderrabano-Gonzalez received the B.S. in Industrial Electronics from the Instituto Tecnológico de Puebla (México), the M.Sc. degree in Electronics from the Instituto Nacional de Astrofísica, Óptica y Electrónica (México), and the Ph.D. in Electrical Engineering from Cinvestav Guadalajara (México); he is currently working as Professor at Universidad Panamericana Campus Guadalajara México. His research interests are Power Electronics, Control of Power Electronic Converters, FACTS devices, and Power Quality.

Dr. Hossam Gaber (Gabbar) is a full Professor in the Department of Energy and Nuclear Engineering, the Faculty of Engineering and Applied Science, at Ontario Tech University (UOIT), where he has established the Energy Safety and Control Lab (ESCL), Smart Energy Systems Lab, and Advanced Plasma Engineering Lab. He is the recipient of the Senior Research Excellence Aware for 2016, UOIT. He is recognized among the top 2 worldwide scientists with high citation in the area of energy. He Fellow IET (FIET) and Distinguished Lecturer – IEEE NPSS on Nuclear-Renewable Hybrid Energy Systems and Plasma-based Waste-to-Energy. He is leading national and international research in the areas of smart energy grids, energy safety and control systems, and waste-to-energy using advanced plasma technologies. Dr. Gabbar obtained his B.Sc. degree in 1988 with first class of honor from the Faculty of Engineering, Alexandria University (Egypt). In 2001, he obtained his Ph.D. degree from Okayama University (Japan). From 2001 till 2004, he joined Tokyo Institute of Technology (Japan), as a research associate. From 2004 till 2008, he joined Okayama University (Japan) as an Associate Professor, in the Division of Industrial Innovation Sciences. From 2007 till 2008, he was a Visiting Professor at the University of Toronto. He also worked as process control, safety, and automation specialist in energy and oil & gas industries. Dr. Gabbar has more than 290 publications, including patents, books / chapters, journal and conference papers.

Vijay K. Sood (Life Fellow, IEEE) received the Ph.D. degree from the University of Bradford, England, in 1977. From 1976 to 2007, he was a Senior Researcher with the Research Institute of Hydro-Québec (IREQ), Montreal. He was also an Adjunct Professor (1984–2007) with Concordia University, Montreal. Since 2007, he has been a Professor with Ontario Tech University, Oshawa. Canada. From 2012 to 2018, he was the NSERC-OPG Design Engineering Co-Chair. He was the Chair of the Department of Electrical and Software Engineering for two years (2021–2023), the Director of the Power Workers Union Smart Grid and EV Research Laboratory, and the Principal Investigator of the Panasonic-UOIT Microgrid. His research interests include monitoring, control, and protection of HVDC and FACTS power systems. He has published over 200 articles in journals and conferences and written two books and numerous book chapters. He is a member of the Professional Engineers of Ontario, a fellow of the Engineering Institute of Canada, and an Emeritus Fellow of Canadian Academy of Engineers. Previously, he has held the following positions: an Editor of the IEEE Transactions on Power Delivery, an Editor of the IEEE Canadian Journal for Electrical and Computer Engineering, and the Chair of the IEEE Canada Awards Committee. He is currently the Editor-in-Chief of the Journal Distributed Generation & Alternative Energy.